International Journal of Heat and Mass Transfer 203 (2023) 123781

Contents lists available at ScienceDirect

International Journal of Heat and Mass Transfer

journal homepage: www.elsevier.com/locate/hmt

Dynamic CFD modeling coupled with heterogeneous boiling for deep two phase closed thermosyphons in artificial ground freezing

Ahmad F. Zueter [a], Muhammad S.K. Tareen [a], Greg Newman [b], Agus P. Sasmito [a,*]

[a] Department of Mining and Materials Engineering, McGill University, 3450 University, Frank Dawson Adams Bldg., Montreal, QC H3A0E8, Canada
[b] Newmans Geotechnique Inc., 311 Adaskin Cove, Saskatoon SK, S7N 4P3, Canada

ARTICLE INFO

Article history:
Received 18 August 2022
Revised 1 December 2022
Accepted 13 December 2022
Available online 26 December 2022

Keywords:
Deep thermosyphons
Artificial ground freezing
Boiling and condensation
Heterogeneous boiling
Bubble nucleation

ABSTRACT

Super-long thermosyphons exceeding 100 m are being employed more frequently in artificial ground freezing (AGF) applications. In this study, we develop a fully-conjugate computational-fluid-dynamics (CFD) model to fundamentally analyze the heat extraction capacity and profile of super-long thermosyphons in AGF. The CFD model couples a heterogeneous condensation/evaporation mass transfer model inside the thermosyphon with thermosyphon-pool hydrostatic pressure distribution and heat diffusion from the ground. The heterogeneous model also considers the kinetic energy required for bubble nucleation and has been validated against experimental studies from the literature. Three main parameters have been investigated: 1) the filling ratio, 2) the charge pressure inside the thermosyphon, and 3) the wind temperature. The results reveal a no-boiling-zone below 10–25 m of pool surface. Further, the charge pressure significantly affect the start-up of the thermosyphon. Lastly, lower wind temperature extracts more heat from the ground in a qualitatively similar manner (similar heat flux profile along thermosyphon wall) to that of higher wind temperature. Overall, the results of this study provide fundamental understanding of the performance of super-long thermosyphons in AGF.

1. Introduction

Two-phase-closed-thermosyphons (TPCT) are heat transfer devices of simple construction with no moving parts. While they have been firstly invented by by Perkin and Buck by the end of the nineteenth century [1,2], Erwin Long (an Alaska based engineer) obtained the US patent for successfully employing TPCT in artificial ground freezing (AGF) systems in 1965 [3]. The first known field installation of these devices dates back to 1960 for foundations stabilization of communication sites at Aurora (Manitoba, Canada) and Glenallen (Alaska, US) [4]. Since then, TPCT have attracted a worldwide interest especially in cold regions due to their passive ability to utilize the available cold wind to freeze the ground. In the 1970s, 120,000 TPCT were installed to support the 800-miles-long Trans-Alaska pipeline built on continuous and discontinuous permafrost regions [5]. In China, 20,000 TPCT were installed between 2006–2009 to raise the permafrost table underlying the 142-km-long Chaidaer-Muli railway [6]. Further, TPCT are widely used across Qinghai-Tibet Plateau, China, to protect the underlying permafrost of railways [7], roadways [8], and power transmission towers [9,10]. The vast majority of present TPCT in permafrost protection applications extend to around 5–30 m below the ground surface. Nevertheless, much deeper TPCT at the Giant Mine Remediation Project are needed to contain arsenic waste stored in underground chambers. Particularly, 706 deep thermosyphon, in addition to 152 shallow ones, will be installed to freeze the ground around the contaminated chambers and, thus, prevent arsenic leakage [11]. The deep TPCT can extend to 100–160 m below the ground surface. The multiphysics boiling and condensation phenomena of deep thermosyphons is different from that of shallow ones.

A TPCT has two main sections: 1) evaporator - embedded in ground and 2) condenser - exposed to cold air. A refrigerant inside the TPCT absorbs heat from the ground in the evaporator section and evaporates as a result. It then flows upwards towards the condenser section, where it exudes the absorbed heat to the ambient air as shown in Fig. 1(a). Upon releasing the heat, it condenses and falls down towards the evaporator section, thus, creating a continuous cycle of heat absorption and release. Thermosyphon-based AGF operation is a multi-scale and multi-physics problem with two aspects: 1) TPCT condensation-evaporation cycle and 2) heat diffusion in the rock. In shallow thermosyphons, the boiling temperature across the evaporator is almost uniform due to the relatively uniform pressure distribution across the liquid pool, which is almost equivalent to the over-

* Corresponding author.
E-mail address: agus.sasmito@mcgill.ca (A.P. Sasmito).

https://doi.org/10.1016/j.ijheatmasstransfer.2022.123781
0017-9310/

Latin letters

A	Area [m^2]
c_p	Specific heat capacity [J kg^{-1} K^{-1}]
f	Friction factor [-]
h	Convective heat transfer coefficient [W m^{-2} K^{-1}]
h_{fg}	Specific latent heat of evaporation [J kg^{-1}]
k	Thermal conductivity [W m^{-1} K^{-1}]
L	Specific latent heat of water freezing/thawing [J kg^{-1}]
m_{tr}	Mass transfer rate from liquid to vapor [kg m^{-3} s^{-1}]
Nu	Nusselt number [-]
Pr	Prandtl number [-]
q	Heat flux [W m−2]
S	Source term (*unit depends on term*)
T	Temperature [K]
u	Velocity [m/s]
t	Time [s]
z	Axial coordinate, where $z = 0$ at the bottom of thermosyphon [m]

Greek letters

ϕ	Porosity [-]
γ	Liquid fraction [-]
ρ	Density [kg m^{-3}]
μ	Dynamic viscosity [Pa s]
α	Phase (liquid/gas) fraction[-]
σ	Surface tension [N/m]

Subscripts

a	Air
e	Evaporatoration
fg	evaporation/condensation
g	Gas state of refrigerant
s	Steel
c	Condensation
ℓ	Liquid state of refrigerant
r	Rock
ref	Refrigerant (in liquid or gas states)
sat	Saturation state
w	Water, in its frozen or unfrozen states

lying vapor pressure. Nonetheless, deeper TPCT contains a much larger liquid pool which linearly increases the hydrostatic pressure along the pool depth. The linear increase in the pressure profile consequently increases the boiling temperature, which creates four unique zones, as shown in Fig. 1(b). The first zone from the top is the condensation zone, adjacent to cold wind where the vapor refrigerant condeses and falls back to the evaporator. The second zone is the film zone, which extracts heat through a liquid film falling towards the pool surface. The third zone is the active pool zone in which the pool boils as heat is extracted from the ground. The hydrostatic pressure increases linearly with pool depth which in turn increases the boiling temperature and slows down the boiling rate. When the boiling temperature exceeds the pool temperature, a dead pool zone is formed, where heat is extracted through conduction and single-phase natural convection.

Previous scientific research has proposed various mathematical models of different complexity to model *shallow* TPCT in AGF systems. A simplified TPCT cycle by Abdalla et al. [12,13] assumes a super-conductor thermosyphon and directly correlates ambient air flow with the heat flux at the evaporator wall. As indicated by results, size of the thaw settlements in the permafrost regions, below warm pipelines, was significantly reduced. A thermal resistance network model was derived by Zhang et al. [14] that

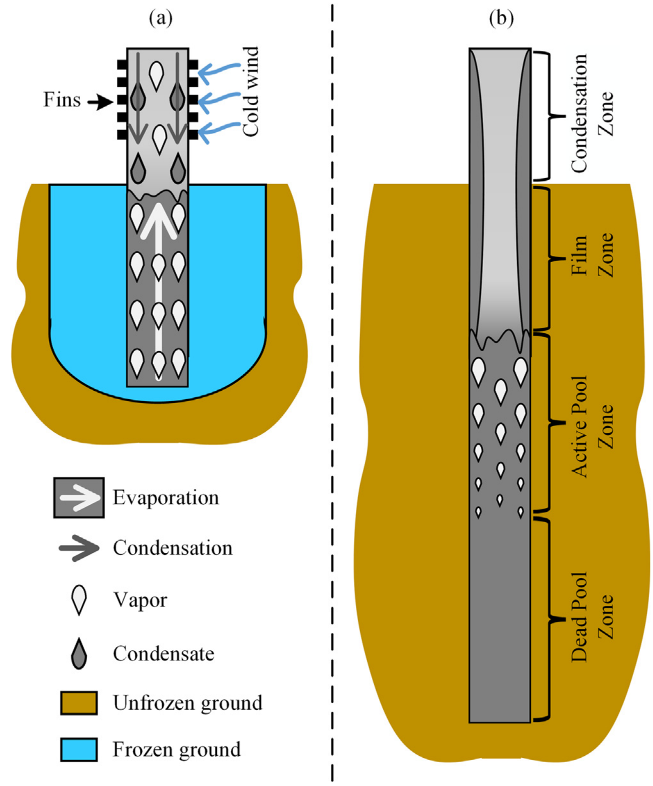

Fig. 1. Not-to-scale schematic illustrating a) the operating principle of passive artificial ground freezing systems using thermosyphons and b) the various heat extraction/dissipation zones in the case of deep thermosyphons.

accounted for the thermal resistance of condensation and evaporation cycles. They demonstrated that the frozen grounds below the Qinghai-Tibet railways and roads are ensured to be protected with TPCT embankment. The thermal resistance network model was extended by Pei et al. [15,16] using L-shaped and inclined TPCT embankments. Yang [17], Cunzhen et al. [18], Yang and Cunzhen [19] used the same thermal network model, but considered a different boiling phenomena in the film-boiling zone. Recently, Zueter et al. [20] derived the first thermal network model for *hybrid* TPCT that run year-round by employing the cold wind in winter seasons and refrigeration plants in warmer seasons. Such numerical studies modeled the expansion of frozen grounds successfully. However, little attention has been given to full-scale modeling of the boiling and condensation phenomena in thermosyphons, especially in AGF applications.

Apart from AGF, thermosyphons have been used as a heat transfer device in several applications such as geothermal energy extraction [21–23] and electronics cooling [24–26]. Accordingly, CFD studies that examine the boiling and condensation phenomena in thermosyphons have been conducted in the literature for various purposes. Alizadehdakhel et al. [27] derived a 2D CFD model for thermosyphons based on the conservation principles of mass, momentum, and energy. The volume-of-fluid (VoF) method [28] is employed to model the equivalent thermophysical properties, as well as the velocity and temperature fields, across the thermosyphon. The evaporation and condensation rate, $S_{v\rightarrow\ell}$, are modeled using Schepper et al. [29] correlation given as

$$S_{v\rightarrow\ell} = \begin{cases} \beta_c\ \chi\ \rho_v\ \alpha_v\ (T_{sat} - T)/T_{sat} & , T < T_{sat}\ \text{(condensation)}; \\ \beta_e\ \rho_\ell\ \alpha_\ell\ (T_{sat} - T)/T_{sat} & , T > T_{sat}\ \text{(evaporation)}, \end{cases} \tag{1}$$

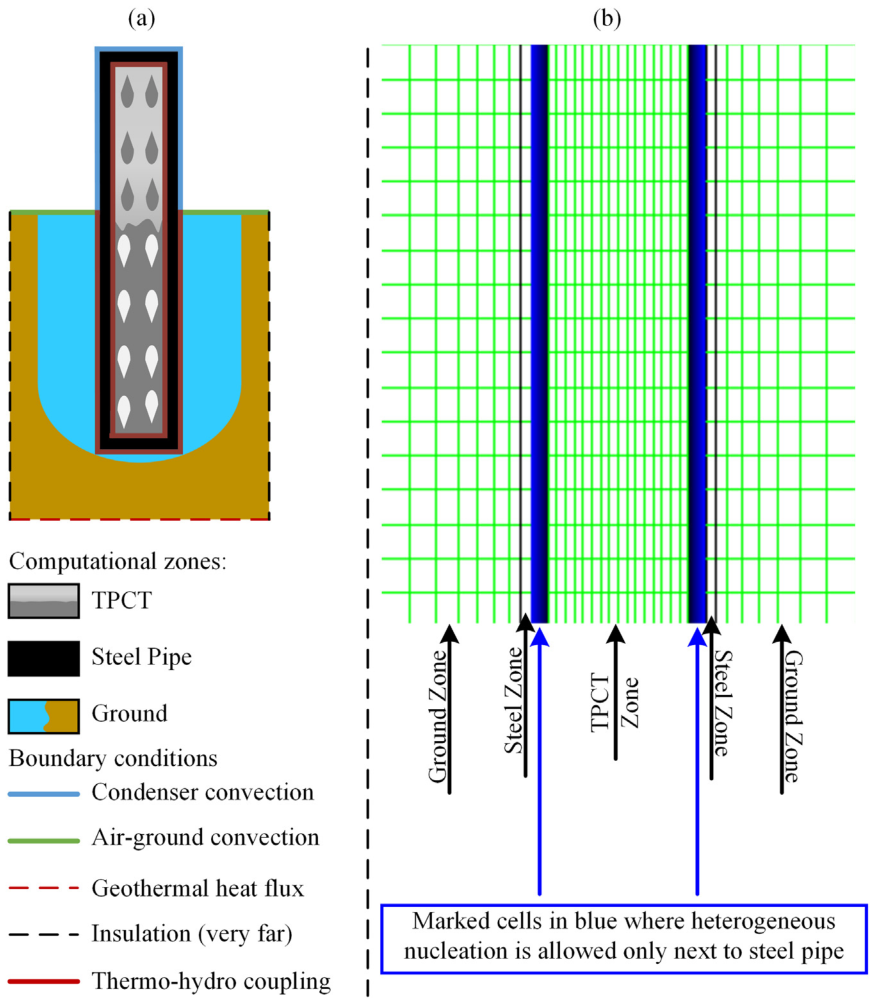

Fig. 2. Not-to-scale schematic illustrating a) the computational zones and their boundary conditions and b) part of the mesh highlighting the heterogeneous boiling conditions where nucleation is only allowed in the marked cells right next to steel pipe.

where ρ, β_c, β_e, χ, α_v, α_ℓ and T represent the density, condensation frequency, evaporation frequency, mole fraction of heat-transfer-fluid inside the thermosyphon (water in Alizadehdakhel et al. [27] experiment), volume fraction of vapor phase, volume fraction of liquid phase, and temperature, respectively. The subscripts v, ℓ, and *sat* refer to vapor phase, liquid phase, and saturation (temperature), respectively. The mole fraction of water is added to the condensation source term due to water's tendency to formulate non-condensable gases. Formation of non-condensable gases can significantly reduce the long-term condenser efficiency as the these gases occupy the top region of the condenser, thus, decreasing the heat exchange area with the condenser heat sink. This was an issue in the operation of ammonia-filled thermoysphons along the Trans-Alaska pipeline. Currently, CO_2 is preferred over ammonia in cold thermosyphon applications due to its chemical stability.

Fadhl et al. [30] used a similar CFD methodology examining water as the working fluid inside the thermosyphon and validated the model against experimental data however without including the mole fraction effect on the condensation. This can be attributed to the short duration of experimental studies as compared to the much longer time needed for formation of non-condensable gases. Fadhl et al. [31] then tested thermosyphon performance with other commercial refrigerants such as R134a and R404a. The bubbles formed in these refrigerants are much smaller than that of water, possibly due to the different critical nucleation site radius. Xu et al. [32] considered the effect surface wettability for mini-thermosyphons in electriconics cooling applications. Kamburova et al. [33] and Abdullahi et al. [34] numerically investigated the impact of the condenser capacity and thermosyphon inclination angle, respectively. Jouhara et al. [35] extended the geometry to 3D in order to observe the geyser boiling phenomena mathematically. Kafeel and Turan [36] derived a more complex Eulerian mathematical model that treats each phase independently.

The discussed CFD studies thus far consider short thermosyphons (less than 10 m) and assume that bubble nucleation is initiated once the liquid temperature exceeds the saturation temperature. Wang et al. [37] conducted a pioneering study which considered the excess temperature needed, dT_i, to form a nucleation site and thus adjusted the evaporation model as

$$S_{\ell\to g} = \begin{cases} \beta_e\rho_\ell\alpha_\ell(T_{sat}-T)/T_{sat} & , 1 > \alpha_g > 0 \text{ and } T > T_{sat}(\text{gas expansion}); \\ 0 & , \alpha_g = 0 \text{ and } T < T_{sat} + dT_i(\text{no nucleation}); \\ \beta_e\rho_\ell\alpha_\ell(T_{sat}-T)/T_{sat} & , \alpha_g = 0 \text{ and } T > T_{sat} + dT_i(\text{nucleation}). \end{cases} \quad (2)$$

This improved model was employed to observe the geyser boiling phenomena of water [37] and investigate lab-scale thermosyphons in shallow geothermal applications using ammonia [38]. After that, Wang et al. [39] derived a novel pressure-based evaporation model based on the Hertz-Knudsen kinetic theory of gases [40]. The pressure-based model also considers the variation of the saturation pressure according to the liquid's temperature. Wang et al. [41] demonstrated that the variation of the saturation pressure in deep thermosyphons can be quite significant in geothermal applications due to the huge hydrostatic pressure accumulating at the bottom of the thermosyphon.

According to the literature presented above, the following research gaps need to be addressed regarding the operation of thermosyphons in artificial ground freezing applications in particular and other applications in general:

- Full-scale CFD models of thermosyphon-based AGF systems using CO_2 have not been conducted yet. Previous AGF literature model thermosyphons using a simplified thermal resistance network model assuming ideal evaporation and condensation. Nonetheless, thermosyphon operation is limited by several operational parameters especially very deep ones such as those operating at the Giant Mine.
- The heterogeneous nature of the boiling phenomena in thermosyphons has not been considered in previous CFD models where nucleation sites should *only* be formed alongside the thermosyphon shell.
- The impact of the initial charge pressure has not yet been investigated for the case of deep TPCTs (even the shallow ones to the best of authors knowledge).
- Lack of CFD models for thermosyphons exceeding 100 m in depth, such as those installed at the Giant Mine.

Thus, the primary purpose of this study is to develop a full-scale CFD model for deep-thermosyphon-based AGF systems coupled with heterogeneous boiling phenomena. Specifically, CFD model for TPCT is initially developed and then validated against the experimental results that are available in the literature. The TPCT CFD model is then coupled with the heat flow in the ground model from our previous work [42,43] that is principally based on enthalpy-porosity method [44]. This model is also extended to field conditions to examine the fundamental and applied impact of three main parameters: 1) thermosyphon filling ratio, 2) thermosyphon charge pressure, and 3) cold wind temperature. This paper is presented with the following sequence of demonstration:

1. Presentation of a mathematical model for TPCT alongside the heat-flow-in-the-ground model.
2. Validation of TPCT model with experimental results from the literature.
3. Examination of the effects of FR, thermosyphon charge pressure (*ICP*) and wind temperature in AGF.

2. Mathematical modeling

A 2D CFD model is built following the conservation principles of mass, momentum, and energy, alongside the heterogeneous bubble nucleation theory. There are three main computational zones: 1) ground occupied by porous rocks, 2) steel pipes, and 3) TPCT filled by a refrigerant, as shown in Fig. 2(a). Mathematical modeling of each zone in addition to their corresponding boundary conditions are provided in the next three subsections.

2.1. Mathematical modeling of the ground

The enthalpy-porosity method has been implemented to calculate the temperature profile of the ground. Local thermal equilibrium (LTE) is assumed due to low porosity of the ground and small difference between thermal conductivity of sand particles and water. Zueter et al. [42] provided an elaborate justification for using LTE in AGF applications as employed in multiple AGF studies [43,45,51]. Thus, the temperature distribution can be calculated using a one-temperature model given as:

Table 1
Thermophysical properties of the materials used in this study. The ground porosity is 1% according to the measurements of the Giant Mine bedrock [47].

Material	ρ [kg/m^3]	c_p [J/(kg·K)]	k [W/(m·K)]	μ[Pa s]
Liquid CO_2 [46]	959	2396	0.117	1.09×10^{-4}
Vapor CO_2 [46]	Ideal gas	1643	18.0×10^{-2}	1.42×10^{-5}
Liquid NH_3 [46]	645	4592	89.1×10^{-2}	1.79×10^{-4}
Vapor NH_3 [46]	Ideal Gas	2613	23.0×10^{-2}	8.19×10^{-6}
Frozen rock [47]	2926	814	3.45	-
Unfrozen rock [47]	2927	822	3.44	-

$$\frac{\partial\left(\overline{\rho_r c_{p,r}} T\right)}{\partial t} = \nabla \cdot \left(\bar{k}_r \nabla T\right) + S, \tag{3}$$

where the subscript r refers to the ground rock and the source term, S, accounts for the latent heat as:

$$S = -\phi \rho_w L_w \frac{\partial \gamma}{\partial t}, \tag{4}$$

where $\rho_w L_w$ is the volumetric latent heat of water, ϕ is the ground porosity, and γ is the liquid fraction. In the mushy zone where both liquid water and ice water coexist, γ is calculated by linear interpolation of the temperature with respect to the solidus and liquidus temperatures. The thermophysical properties of ground and water can be found in Table 1.

The ground zone is enclosed by several boundaries, as shown in Fig. 2(a). On the top, the ground is subjected to atmospheric heat convection given as

$$-\bar{k}_r \frac{\partial T}{\partial n}\bigg|_{top\ \ boundary} = h\left(T|_{top\ \ boundary} - T_a\right), \tag{5}$$

where T_a is the air temperature, h is the atmospheric heat transfer coefficient, and n is a normal vector to the boundary. One the sides, a boundary independent insulation is modeled 0.5 m away from the thermosyphon, so that the temperature distribution in the vicinity of the thermosyphon is not affected by the side boundaries. This is mathematically expressed as:

$$\frac{\partial T}{\partial n}\bigg|_{side\ \ boundaries} = 0. \tag{6}$$

Geothermal heat flux at the bottom boundary is set as:

$$-\bar{k}_r \frac{\partial T}{\partial n}\bigg|_{bottom\ \ boundary} = 0.06[\mathrm{W/m^2}] \tag{7}$$

Finally, thermal coupling between the ground zone and the steel zone is given as:

$$\bar{k}_r \frac{\partial T_r}{\partial n}\bigg|_{pipe-ground} = k_s \frac{\partial T_s}{\partial n}\bigg|_{pipe-ground} \tag{8}$$

where the subscript s refers to the steel zone.

2.2. Mathematical modeling of the steel pipe

Heat flow in the steel is calculated as:

$$\frac{\partial\left(\rho_s c_{p,s} T\right)}{\partial t} = \nabla \cdot \left(k_s \nabla T\right) \tag{9}$$

The outer wall of the steel pipe in the evaporator section is in contact with the ground. Coupling between the ground and the steel

Table 2
Summary of boiling and condensation cases of Eq. (13).

Case 1:	Expansion (or contraction) of an already developed bubble.
Case 2:	Bubble nucleation is not allowed until reaching the nucleation temperature.
Case 3:	Homogeneous nucleation within the bulk liquid is not allowed.
Case 4:	Heterogeneous nucleation: Bubble nucleation is only allowed on a solid surface.
Case 5:	Condensation

pipe is already shown in Eq. (8). In the condenser section above the ground level, convective heat of the wind is modeled as:

$$h\ (T_{cw} - T_a) = k_s \frac{\partial T_s}{\partial n}\bigg|_{cw} \tag{10}$$

where h is the heat transfer coefficient of the wind approximated at 150 [W/(m^{2}K)], T_∞ is the wind temperature, and subscript *cw* refers to the outer condenser wall. In this study, three cases of wind temperature are considered: 1) -15 [°C], 2) -20 [°C], and 3) -30 [°C]. Along the inner walls of the TPCT, the steel pipe zone is thermally coupled with the TPCT zone as:

$$k_{ref} \frac{\partial T_{ref}}{\partial n}\bigg|_{pipe-TPCT} = k_s \frac{\partial T_s}{\partial n}\bigg|_{pipe-TPCT} \tag{11}$$

where the subscript *ref* refers to the operating refrigerant.

2.3. Mathematical modeling of the TPCT

Novelty of this work lies in its capability to fully couple the evaporation and condensation cycles of the TPCT with ground freezing. The volume-of-fluid (VoF) model has been adapted in this study due to its superior computational efficiency over other CFD techniques for modeling evaporation and condensation. In addition, the VoF model has demonstrated sufficient reliability in many TPCT studies for non-AGF systems.

The VoF model expresses the continuity of the refrigerant with two equations for the 1) liquid phase and 2) vapor phase. Continuity equation of the liquid phase is given as:

$$\frac{\partial}{\partial t}(\rho_\ell \alpha_\ell) + \nabla \cdot (\alpha_\ell \rho_\ell \vec{u}) = -m_{tr}, \tag{12}$$

where $\vec{u}$ is the velocity field and α_ℓ is the liquid fraction of the refrigerant (not to be confused with γ and ϕ which are correlated to the ground domain) whereas subscripts ℓ and v denote the liquid phase and vapor phase, respectively. The liquid to vapor mass transfer source term (boiling/condensation rate), depends on the nucleation temperature, T_{nuc}, which relies on pressure-dependent saturation temperature $T_{sat} = f(P)$. Heterogeneous bubble nucleation, in which bubbles are formed on the wall surface, prevails over homogeneous bubble nucleation, where bubbles are formed inside the bulk of the liquid [48]. This is attributed to the high required rate of nuclei formation (exceeding 10^{12} [nuclei cm^{-3}s^{-1}]) for the case of homogeneous boiling [48]. Accordingly, in this study, bubble nucleation is allowed only on computational nodes attached to the solid surface, as shown in Fig. 2(b).

The mass transfer source term is thus calculated according to five different cases as per Eq. (13) and Table 2.

where β_e and β_c are the evaporation and condensation frequency, respectively, and subscript v refers to vapor state.

The saturation temperature is determined by curve-fitting the temperature-pressure saturation curve [46] as:

$$T_{sat}(P) = c_1\ P^4 + c_2\ P^3 + c_3\ P^2 + c_4\ P + c_5, \tag{14}$$

where the coefficients c_1 through c_5 can be found in Table 3.

Rohsenow [49] determined the nucleation temperature following a semi-analytical derivation as

$$T_{nuc} = T_{sat} + Pr_\ell \sqrt{\frac{8\sigma T_{sat} q}{h_{fg}\rho_g k_\ell}} \tag{15}$$

As there are only two phases in the thermosyphon, the vapor volume fraction, α_g, in Eq. (13) is the compliment of the liquid fraction, α_ℓ, as:

$$\alpha_g = 1 - \alpha_\ell \tag{16}$$

The conservation of momentum is given as:

$$\frac{\partial\left(\rho_{ref}\ \vec{u}\right)}{\partial t} + \nabla \cdot \left(\rho_{ref}\ \vec{u}\ \vec{u}\right) = -\nabla P + \nabla \cdot \left[\mu_{ref}\left(\nabla\ \vec{u} + \nabla \vec{u}^{T}\right)\right] + \rho_{ref}\ \vec{g} + S_{st} \tag{17}$$

where $\vec{g}$ is the gravitational acceleration and S_{st} is the surface tension source term. The thermosyphical properties of the refrigerant are set according to the phase of the each computational node as listed in Table 1. Nonetheless, the density of the vapor phase is assumed to obey the ideal gas law. When both liquid and vapor phases exist together in the same computational node, the thermophysical properties are calculated based on volume averaging.

The energy conservation is expressed as:

$$\frac{\partial\left(\rho_{ref} c_{p,ref} T\right)}{\partial t} + \nabla \cdot \left(\rho c_{p,ref} T\ \ \vec{u}\right) = \nabla \cdot \left[k_{ref}(\nabla T)\right] + S_{fg}, \tag{18}$$

where the source term, S_{fg}, is added to incorporate the latent heat of vaporization and is calculated with respect to the mass transfer source term, m_{tr}, as:

$$S_{fg} = -m_{tr}\ h_{fg}, \tag{19}$$

where h_{fg} is the specific latent heat of the refrigerant.

The refrigerant is fully bounded by the steel shell. Thermal coupling between the refrigerant and the steel shell is given in Eq. (11). Further, a no-slip condition is imposed as

$$\vec{u}|_{steel\ \ wall} = 0 \tag{20}$$

$$m_{tr} = \begin{cases} \beta_e \rho_\ell \alpha_\ell (T - T_{sat})/T_{sat} & , \alpha_\ell < 1 \text{ and } T > T_{sat} \text{ (case 1);} \\ 0 & , \alpha_\ell = 1 \text{ and } T < T_{nuc} \text{ (case 2);} \\ 0 & , \alpha_\ell = 1 \text{ and } T > T_{nuc} \text{ and none-wall cell(case 3);} \\ \beta_e \rho_\ell \alpha_\ell (T - T_{sat})/T_{sat} & , \alpha_\ell = 1 \text{ and } T > T_{nuc} \text{ and wall-cell(case 4);} \\ \beta_c \rho_g \alpha_g (T - T_{sat})/T_{sat} & T < T_{sat} \text{ (case 5);} \end{cases} \tag{13}$$

Table 3
The coefficients of Eq. (14), as curve-fitted from NIS [46].

Material	c_1 [K/Pa^4]	c_2 [K/Pa^3]	c_3 [K/Pa^2]	c_2 [K/Pa]	c_5 [K]
CO_2	-8.049$\times10^{-26}$	1.285$\times10^{-18}$	-8.645$\times10^{-12}$	3.8$\times10^{-05}$	203
NH_3	-6.656$\times10^{-24}$	4.238$\times10^{-17}$	-1.016$\times10^{-10}$	1.32$\times10^{-4}$	232

3. Numerical method

A two-dimensional implicit CFD model was developed with the aid of ANSYS FLUENT/18.1 to compute the mathematical model as prescribed by the governing equations and boundary conditions. The non-iterative-time-advancement (NITO) scheme is used in this study where velocity, pressure, and temperature undergo seperate inner iterations rather than large outer iteration loops. This aspect of the NITO scheme significantly reduces its computational time, which is highly desirable in our simulations where each case lasts for around six months of computational time due to the small time step of 0.01s required for solution convergence. Furthermore, the governing equations were discretized by second-order schemes in space and explicit first-order schemes in time. The convergence criteria of the continuity and momentum equations were set at 1E-4 whereas that of the energy equation was set at 1E-8. A mesh independence study is conducted and ensured in this study. Specifically, we tested our simulations at four different mesh sizes at 1) 237,142 nodes, 2) 387,618 nodes, 3) 411,306 nodes, and 4) 529,746 nodes. The computational time of these cases range between three to six months. The results show that the heat extraction rate at the evaporator section is mesh independent at a mesh size of 387,618 nodes. The heat extraction rate at this mesh size is found to be within 10% of that at a mesh size of 529,746 (and 8% of that at mesh size of 411306).

4. Results and discussion

In this section, the mathematical model is firstly validated against experimental measurements. Then, the impact of the following operational parameters on the performance of thermosyphons in field-scale conditions is examined: 1) filling ratio of the working fluid, 2) charge pressure, and 3) air temperature. In all field simulations, apart from validation in Section 4.1, the thermosyphon is filled with pressurized CO_2. Furthermore, the length of thermosyphon evaporator, adiabatic, and condenser sections is set to: 100 m, 2 m, and 6.27 m, respectively, as per field thermosyphons data [20,50]. The thermosyphon diameter is 10 cm. In field conditions, the ground is initialized at a temperature of 1[$^\circ$C], whereas the initial thermosyphon temperature is set equal to the saturation temperature of the thermosyphon charge pressure, which is 2.5[MPa] unless otherwise stated. Additionally, the wind temperature is set at -20 [$^\circ$C], except in the last subsection, where it is varied from -30 [$^\circ$C] to -15 [$^\circ$C]. The base fill-ratio is also set at 75% unless otherwise stated.

4.1. Model validation

The mathematical model of this study includes two main parts: 1) The ground freezing model using the enthalpy method, and 2) The VOF model of TPCT using the Lee model. The former of these parts have been validated in our previous work [42]. Thus, this subsection is dedicated to validate the VOF model. The experimental and mathematical study of Wang et al. [37] was selected for validation purposes.

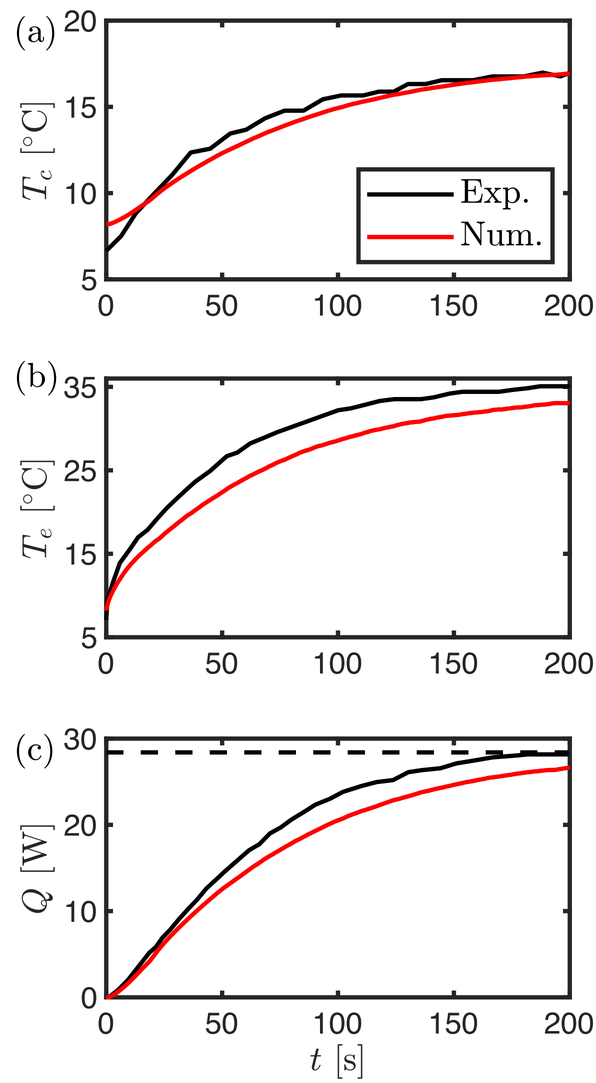

Fig. 3. Validation of the numerical model against the experimental measurements of Wang et al. [37]: a) condenser wall temperature, b) evaporator wall temperature, and c) heat extraction at the condenser (the dashed line represents the input heat transfer rate at the evaporator section in the experiment and model).

The experimental setup is composed of a Ø9 $\times$ 1 [mm] cylindrical thermosyphon filled with ammonia. The lengths of the evaporator, adiabatic, and condenser sections are 20 cm, 10 cm, and 20 cm, respectively. The evaporator is subject to fixed heat flux of 5026.6 [W/m^2] whereas, the condenser is cooled by a flow of water having an overall heat transfer coefficient of 539 [W/(m^{2}K)] and temperature of 8.2 [$^\circ$C]. As can be seen from Fig. 3, the experiment was initialized at a temperature of around 8 [$^\circ$C] and lasted for 200 [s]. The average temperature of the evaporator and condenser were determined using eight thermocouples installed along

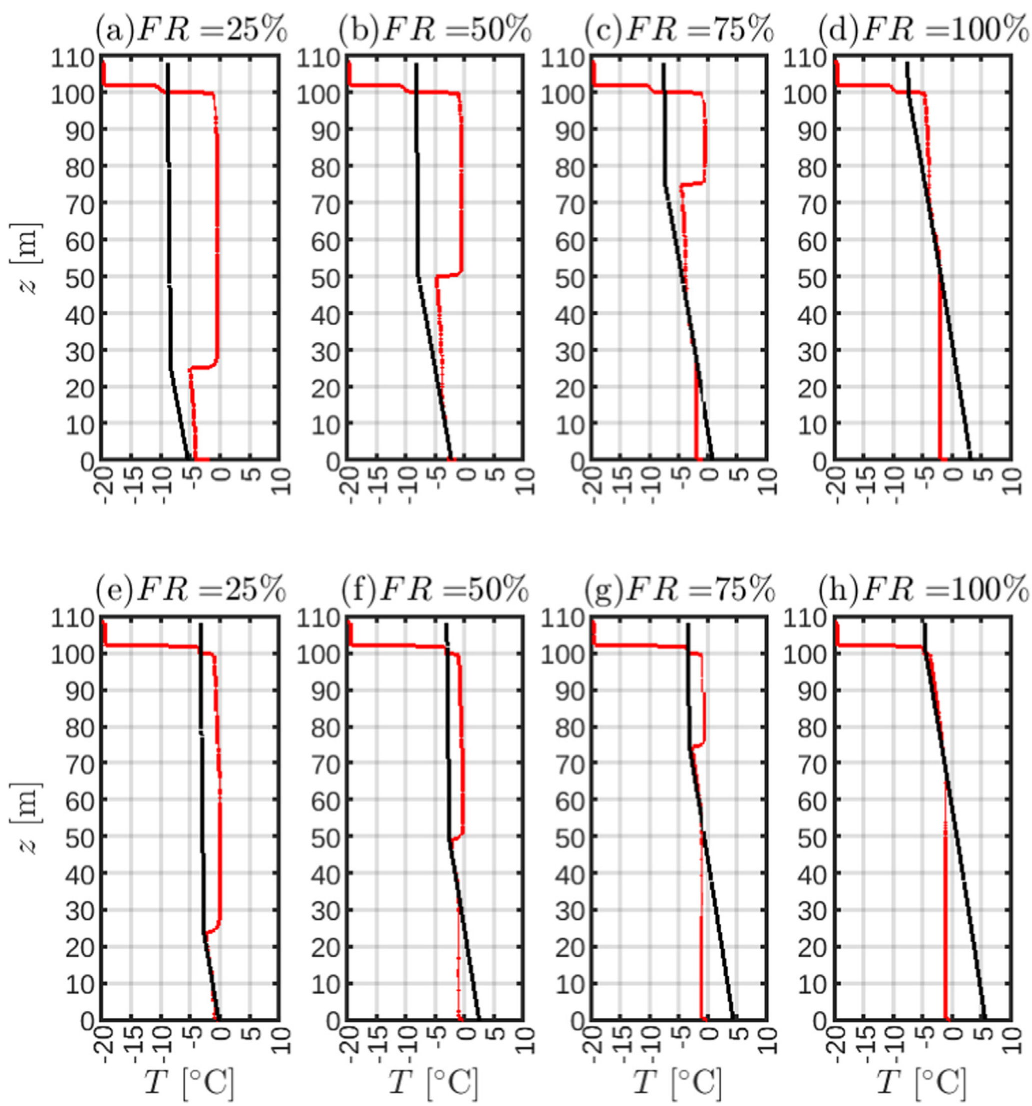

Fig. 4. Thermosyphon wall temperature (in red) and nucleation temperature (in black) along the thermosyphon wall at different filling ratios. Subplots (a-d) are plotted after one hour of operation, whereas subplots (e-h) are plotted after 10 h of operation. The bottom of the thermosyphon is considered as a reference point at $z = 0$; thus, the ground level is at $z = 100$ [m]. (For interpretation of the references to colour in this figure legend, the reader is referred to the web version of this article.)

the wall. Our numerical model agrees well with the experimental data, as shown in Fig. 3.

4.2. Impact of thermosyphon filling ratio

In this subsection, the impact of filling ratio of CO_2 inside a 100 m deep thermosyphon is investigated in AGF systems. The filling ratio is the initial volume of liquid CO_2 divided by the volume of the evaporator. Four filling ratios are investigated in the present study: $FR = 100\%$, $FR = 75\%$, $FR = 50\%$, and $FR = 25\%$, as shown in Figure 7.

The filling ratio evidently impacts the axial distribtion of the nucleation temperature, T_{nuc}, as can be seen in Fig. 4. While T_{nuc} is uniform above the pool level, hydrostatic pressure of the liquid column causes the nucleation temperature to increase linearly at a rate of 0.125 [K] per meter depth of the pool. Accordingly, increase in the nucleation temperature across the pool is linearly proportional to the filling ratio. For instance, after one hour of operation, the nucleation temperature at $FR = 25\%$ has decreased by around 3 [K] from the pool surface at $z = 25$[m] to the bottom of the thermosyphon. On the other hand, in the case of $FR = 100\%$, the nucleation temperature has increased by around 12 [K] from the pool surface at $z = 100$[m] to the bottom of the thermosyphon. It is also observed that the nucleation temperature increases with time. For instance, by comparing Fig. 4(a) with (e), the nucleation temperature line shifts to the right by around 6 [K]. As the thermosyphon extracts heat from the ground, the temperature and pressure inside the thermosyphon increases, which in turn also increases the nucleation temperature.

The proportional increase of T_{nuc} along the thermosyphon depth substantially affects the boiling phenomena inside the pool. At a filling ratio of 25% in the first hour, the wall temperature is always higher than the nucleation temperature - indicating that boiling occurs throughout the pool depth, as shown in Fig. 4(a). How-

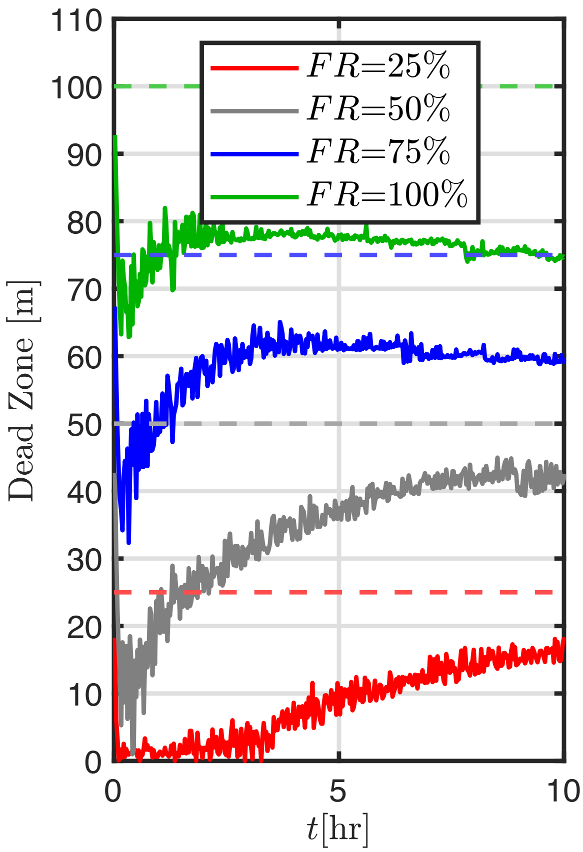

Fig. 5. Extent of dead zone in the thermosyphon at different filling ratios through the first 10 h of operation - the dashed lines represent the pool surface given each filling ratio.

ever, as the filling ratio increases, the wall temperature intersects with the nucleation temperature at higher axial positions - creating larger *dead zones* where boiling does not occur, as schematically illustrated in Fig. 1(b). The axial position of the pool dead zone increases in the first hours as the thermosyphon approaches steady state, as can be seen in Fig. 5. Thermosyphons with higher filling ratios approach a steady state faster than the lower ones due to the less distance needed for the vapor volume to travel from the pool surface to the condenser. While the dead zone is proportional to the filling ratio, the active pool zone tends to be nonetheless larger at higher filling ratios. The effect of the dead zone on the boiling rate as well as the heat flux along the thermosyphon wall is evident in Fig. 6(a-d). At higher filling ratios, no boiling occurs at the bottom of the thermosyphon until the wall temperature is higher than the nucleation temperature near the pool surface. Nonetheless, the boiling rate in the active zone at higher filling ratios after 10 h of operation, is found to be higher than that of the lower ones due to the feedback from the condenser. As for the film zone, the boiling rate is found to be negligible, compared to that of the pool zone.

The dead zone is further illustrated by visualizing the vapor fraction, α_g, at the evaporator section in Fig. 7 for different filling ratios. At $FR = 100\%$, the dead-zone is observed at a depth of around 25 m below the ground surface, as shown in Fig. 7(b,c) where vapor fraction α_g reaches zero at $z \sim 75$ [m]. Similarly, the deadzone is observed to be around 20 m deep in the remaining cases. Nevertheless, at filling ratio of 50% and 25%, the deadzone becomes larger after six hours (smaller boiling zone). This is attributed to the slow evaporation/condensation cycle due to the long distance between the pool surface and the condenser section. The pool surface level is even noted to slightly decrease in these scenarios due to the slow feedback from the condenser.

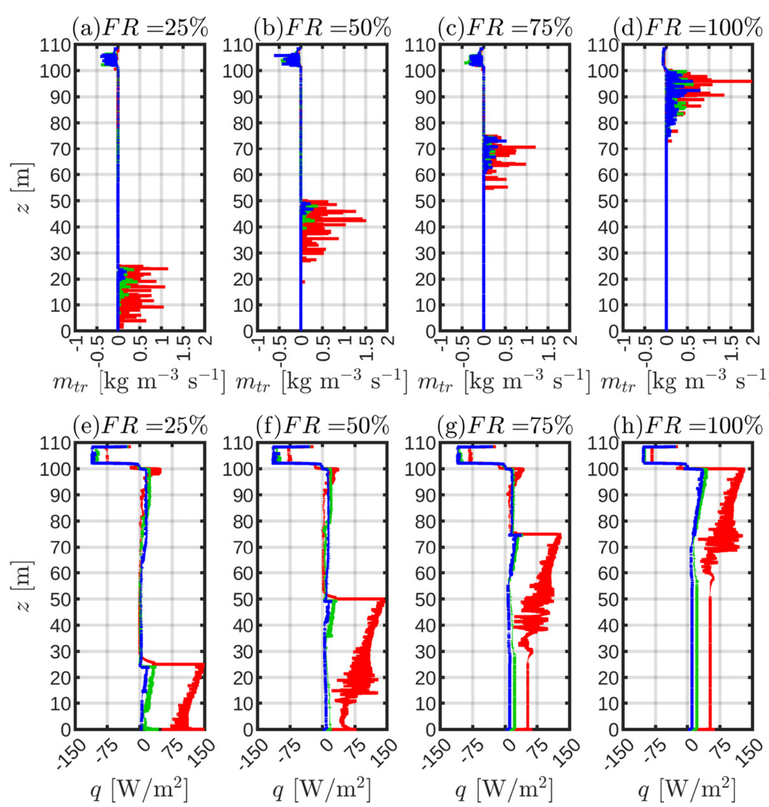

Fig. 6. Mass transfer rate and heat flux along the thermosyphon wall at different filling ratios (positive mass transfer rate denotes evaporation while negative mass transfer rate represents condensation). The red, green, and blue lines are plotted after one hour, five hours, and 10 h of operation, respectively. (For interpretation of the references to colour in this figure legend, the reader is referred to the web version of this article.)

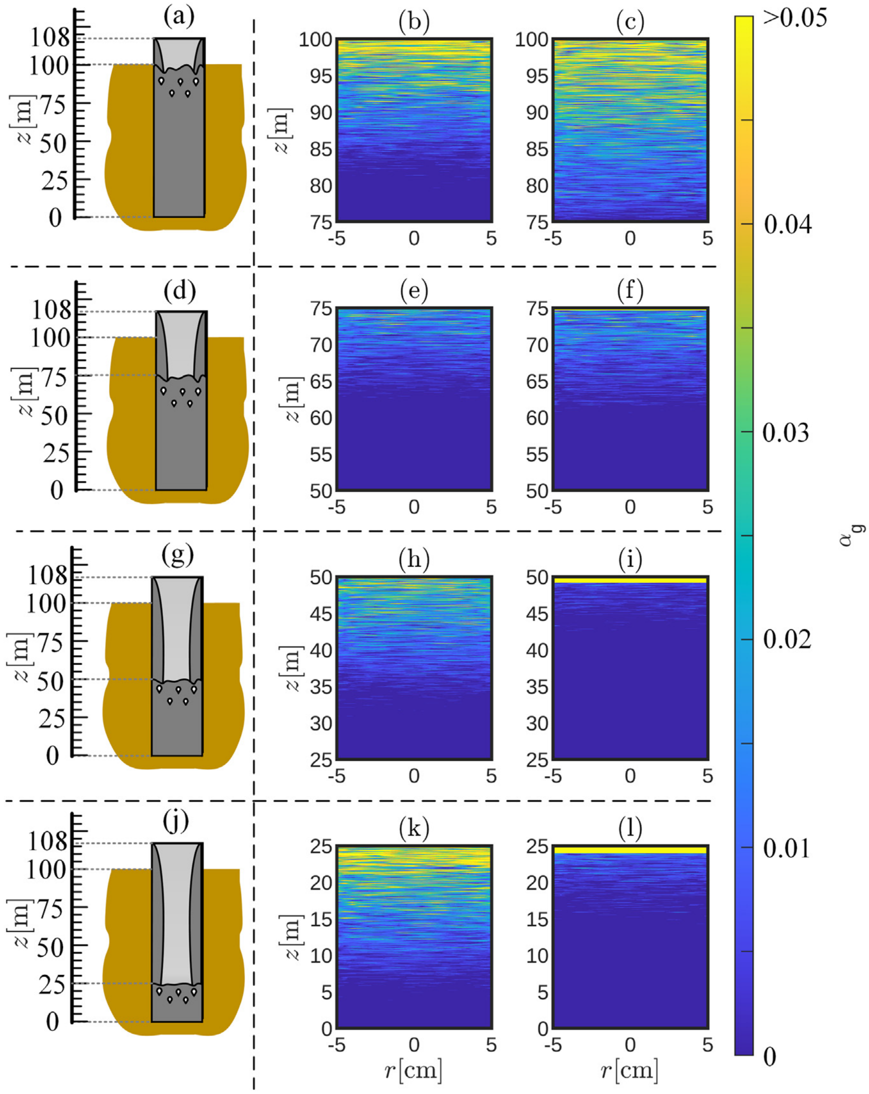

Fig. 7. Boiling phenomena at different filling ratios: subplots (a), (d), (g), and (j) are schematic illustration for filling ratios of 100%, 75%, 50%, and 25%. It should be noted that the axial reference is set at the bottom of thermosyphon ($z = 0$ at thermosyphon bottom), and ground surface is therefore located at $z = 100$ [m] for our cases. Subplots (b), (e), (h), and (k) are plotted after one hour of operation for filling ratio of 100%, 75%, 50%, and 25%, respectively. Subplots (c), (f), (i), and (l) are plotted after six hours of operation for filling ratio of 100%, 75%, 50%, and 25%, respectively.

To further examine the condensation cycle, Fig. 8 shows vapor fraction and velocity vectors at the condenser section. In the first hour, a liquid film is observed along the walls of the condenser. The liquid film remains at a filling ratio of 100% due to the frequent availability of vapor. Nonetheless, at smaller filling-ratios, as there is little vapor circulation, the temperature of the entire condenser section decreases. This leads to condensation within the bulk of the condenser as well as the walls.

The axial heat extraction profile heavily relies on the the relationship between the filling ratio and the boiling rate, as can be seen in Fig. 6(e–h). In the dead zone, the heat flux is uniform - implying that heat is mainly extracted by conduction. On the other hand, in the active zone, the heat flux fluctuates due to boiling phenomena but increases near the pool surface due to the lower nucleation temperature in that region. The fluctuations are essentially formed by the non-uniform bubble nucleation across the evaporator at each instant. In other words, where a bubble is forming, there is a high mass transfer rate and a high heat flux. At the same instant, where a bubble is not forming yet at a different point along the evaporator, the heat flux is lower. Thus, depending on the bubble nucleation stage at each location across the evaporator, mass transfer rate fluctuates and accordingly heat flux fluctuates. In all cases, the boiling rate and heat extraction capacity decrease with time - as the ground temperature decreases. Nevertheless, the heat flux profile of the film zone becomes larger with time, indicating that the film is developing. At a filling ratio of 75%, heat extraction is observed throughout the film zone, as shown in Fig. 6(g). On the other hand, at a filling ratio of 25%, the depth of the heat extraction profile in the film zone is increased to 40 m ($z = 60$ [m]) after of 10 h of operation.

The amount of heat extracted in each zone depends on the filling ratio, as can be seen in Fig. 9. Evidently, heat extracted in the film-zone is inversely proportional to the filling ratio down to $FR = 50\%$, indicating that the film cold energy is utilized around

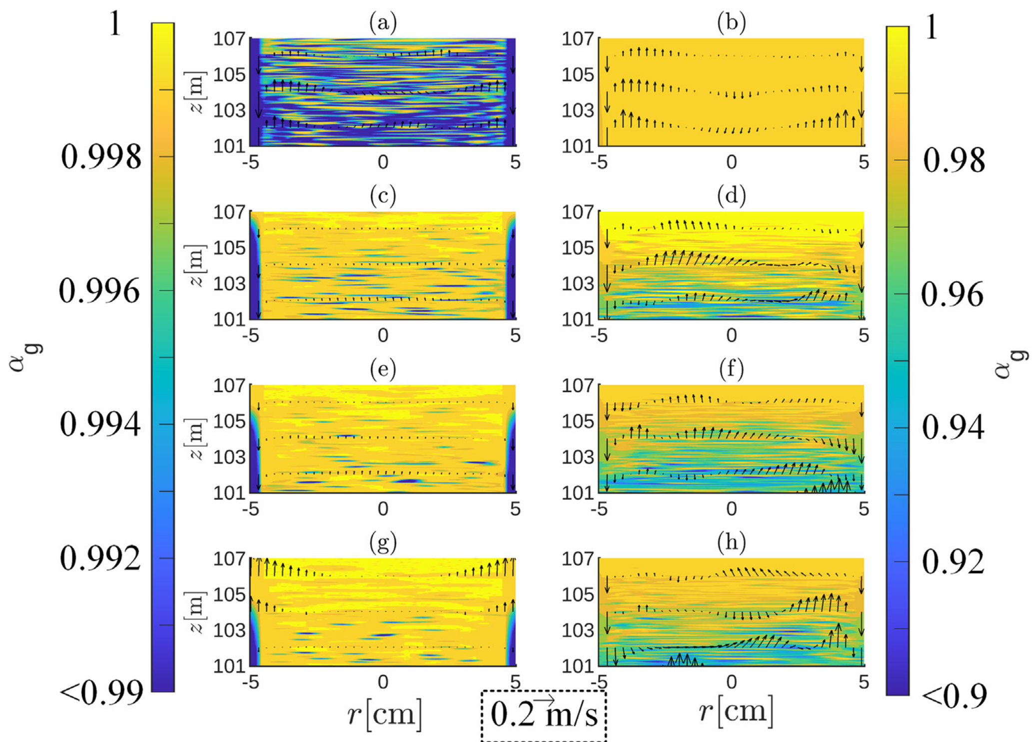

Fig. 8. Condensation phenomena at different filling ratios: Subplots (a), (c), (e), and (g) are plotted after one hour of operation for filling ratio of 100%, 75%, 50%, and 25%, respectively. Subplots (b), (d), (f), and (h) are plotted after six hours of operation for filling ratios of 100%, 75%, 50%, and 25%, respectively. Please refer to Figure 8 for further schematic illustration.

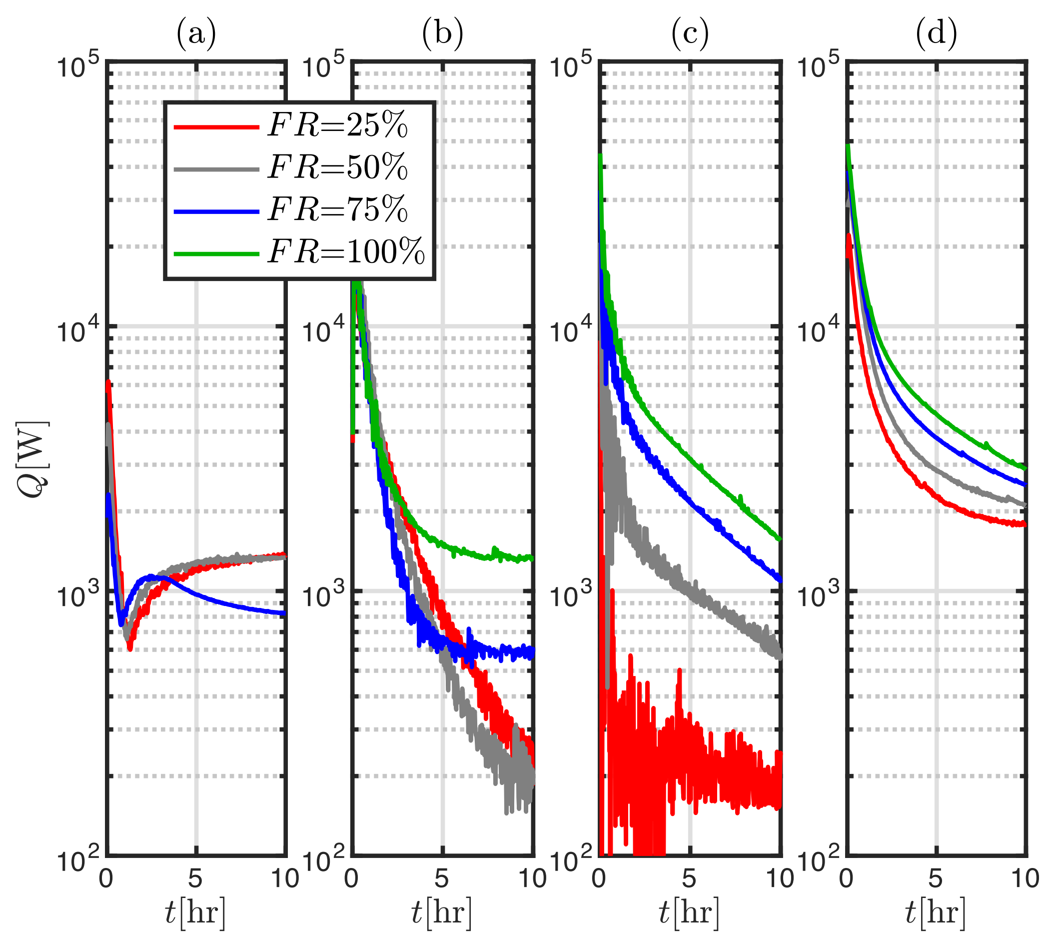

Fig. 9. Heat transfer rate at different filling ratios in the a) film zone, b) active pool zone, and c) dead pool zone, in addition to the d) total heat transfer rate.

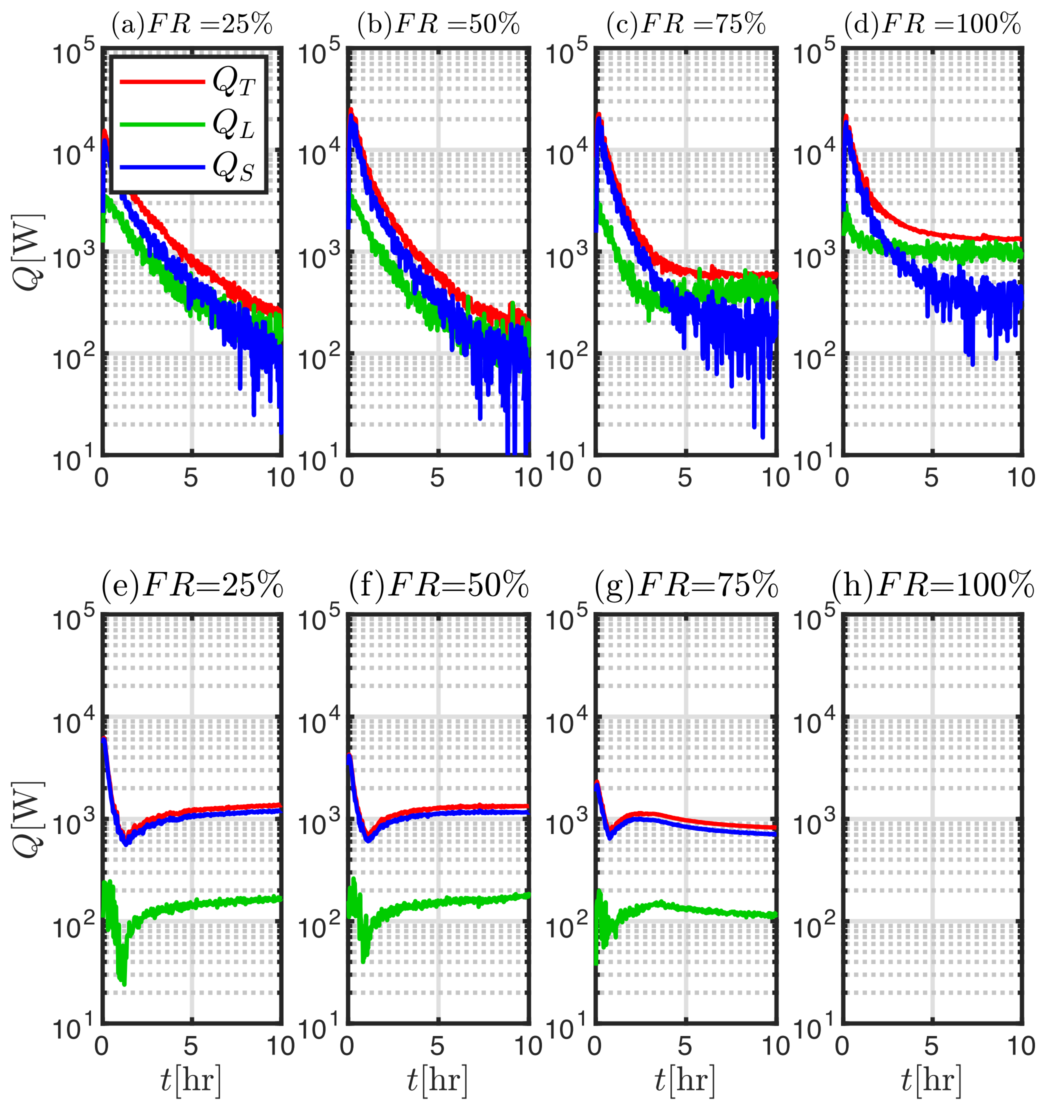

Fig. 10. Modes of heat transfer at different filling ratios where Q_S, Q_L, and Q_T represent sensible heat transfer, latent heat transfer, and total heat transfer, respectively. Subplots (a-d) are calculated at the active pool zone, whereas subplots (e-g) are calculated at the film zone (there is no film zone at $FR = 100\%$).

a depth of 50 m, as can be seen in Fig. 9(a). On the other hand, the pool active zone is proportional to the filling ratio down to $FR = 50\%$, below which the effect of the filling ratio becomes negligible, as can be seen in Fig. 9(b). Also, as for the dead pool zone, the amount of heat extracted is larger at higher filling ratios due to the larger volume of the dead zone, as can be seen in Fig. 9(c). Nevertheless, heat extracted at the dead zone decreases exponentially and is expected to have a minimal contribution once the thermosyphon approaches a steady state. Overall, after 10 h of operation, the amount of heat extracted is proportional to the filling ratio, as shown in Fig. 9(d).

Heat extracted in each zone can be in the form of latent heat or sensible heat, as can be seen from Fig. 10. In the active pool zone, sensible heat is *initially* higher than latent, as shown in Fig. 10(a-d). However, as thermosyphons approach steady state, latent form of heat becomes more dominant than sensible heat. This happens more rapidly at higher filling ratios because of the faster feedback from the condenser which accelerates the steady-state behavior. As for the film zone, it can be seen that sensible heat is much more dominant than latent heat.

4.3. Impact of thermosyphon charge pressure

The charge pressure of the thermosyphon can significantly influence the initial saturation temperature along the depth of the thermosyphon, as seen in Fig. 11. For instance, initializing the thermosyphon at a pressure of 1.5 [MPa] results in an initial vapor saturation temperature of -16.6[°C]; however, an initial charge pressure of 3.5 [MPa] results in a vapor saturation temperature of -1[°C], as shown in Fig. 11(a,c). After ten hours of operation the vapor saturation temperature increases substntially at the cases of low initial charge pressure. Particularly, at an initial charge pressure of 1.5 [MPa], the vapor saturation temperature has increased by 11 [K] (from -16 [°C] to -5 [°C]), as shown in Fig. 11(a,d). At a charge pressure of 2.5 [MPa], the vapor saturation temperature also increased but by 5 [K] only, as shown in Fig. 11(b,e). Interestingly,

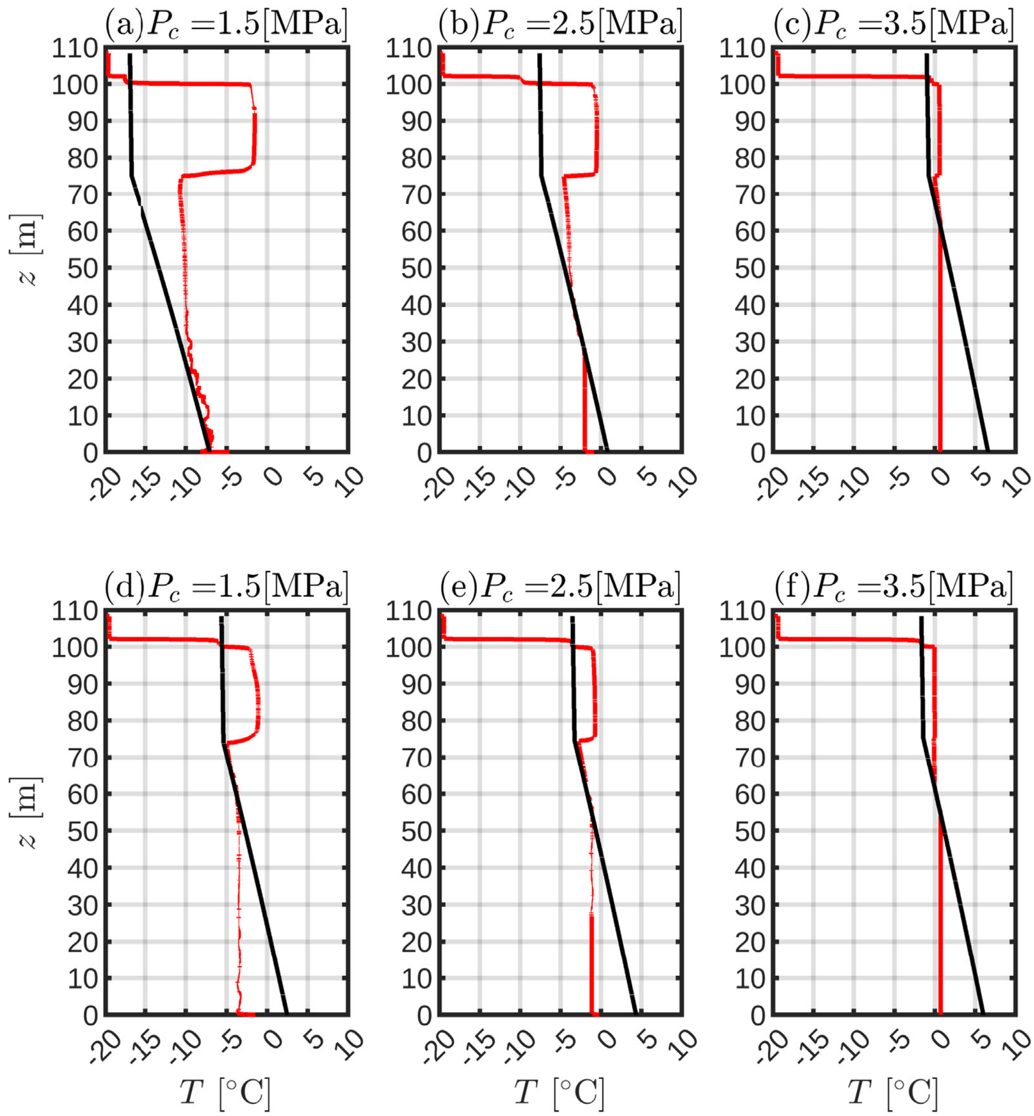

Fig. 11. Thermosyphon wall temperature (in red) and nucleation temperature (in black) along the thermosyphon wall at different charge pressures. Subplots (a-c) are plotted after one hour of operation, whereas subplots (d-f) are plotted after 10 h of operation. The bottom of the thermosyphon is considered as a reference point at $z = 0$; thus, the ground level is at $z = 100$ [m]. (For interpretation of the references to colour in this figure legend, the reader is referred to the web version of this article.)

at even higher initial pressure of 3.5 [MPa] the vapor saturation temperatures slightly *decreases* by 1 [K]. Apparently, as the three cases approach steady state, the saturation temperature line converge to the same profile. The higher initial temperature difference at lower charge pressure results in a higher initial evaporation rate and heat flux, as can be seen in Fig. 12. This leads to a lower wall temperature, as shown in Fig. 11(c), which causes the evaporation rate and heat flux to decrease significantly after longer periods. As shown in Fig. 13, the dead zone at lower charge pressure is initially lower than that at higher pressures, but becomes larger with time as the wall temperature decreases and the saturation temperature increases. Another important observation from Fig. 12 is the more stable start-up of the thermosyphon at higher charge pressure. At lower charge pressures of 1.5[MPa] and 2.5[MPa], the heat extraction rate is very high initially and then decreases with time. On the other hand, at initial charge pressure of 3.5 [MPa], the heat extraction rate increases slowly and progressively, which is preferable on starting-up the thermosyphon. This is possibly the reason that field thermosyphons at the Giant Mine can be charged up to 5 [MPa] [11].

Similar qualitative trends are observed in different heat extraction zones along the thermosyphon at initial charge pressure of 1.5 [MPa] and 2.5 [MPa], as shown in Fig. 14. In the film zone, the amount of heat extracted is similar in both scenarios, as shown in Fig. 14(a). The initial fluctuation of heat flux at a charge pressure of 1.5[MPa] is attributed to very low feedback from the condenser in the first few hours, as implied in Fig. 12(a), due to the low saturation temperature of condensation at lower charge pressure. For an initial charge pressure of 3.5 [MPa], the initial heat extraction rate is almost negligible due to the low thermal gradient between the initial vapor saturation temperature and the ground. As film feedback develops from the condenser, the heat extraction rate in-

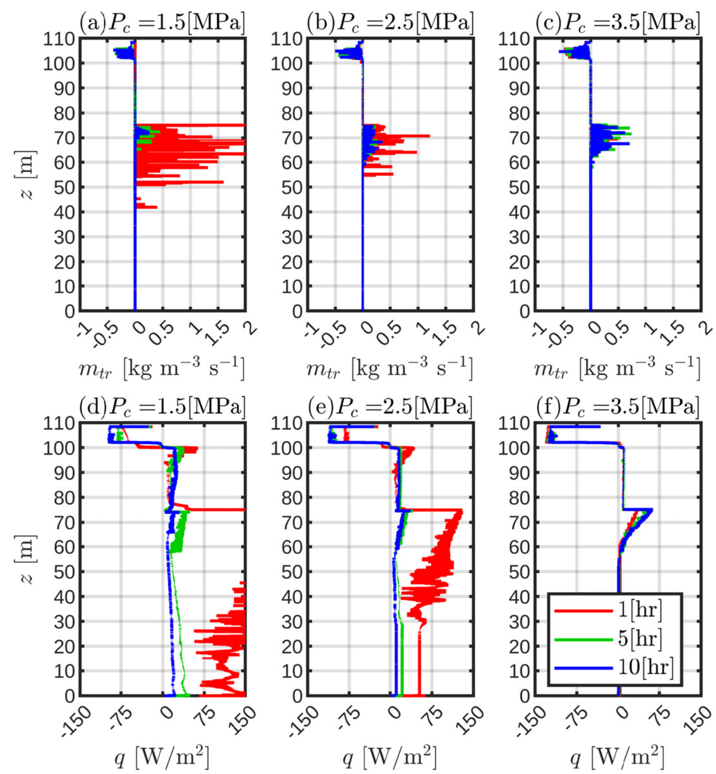

Fig. 12. Mass transfer rate and heat flux along the thermosyphon wall at different charge pressure. (positive mass transfer rate denotes evaporation while negative mass transfer rate represents condensation). The red, green, and blue lines are plotted after one hour, five hours, and 10 h of operation, respectively. (For interpretation of the references to colour in this figure legend, the reader is referred to the web version of this article.)

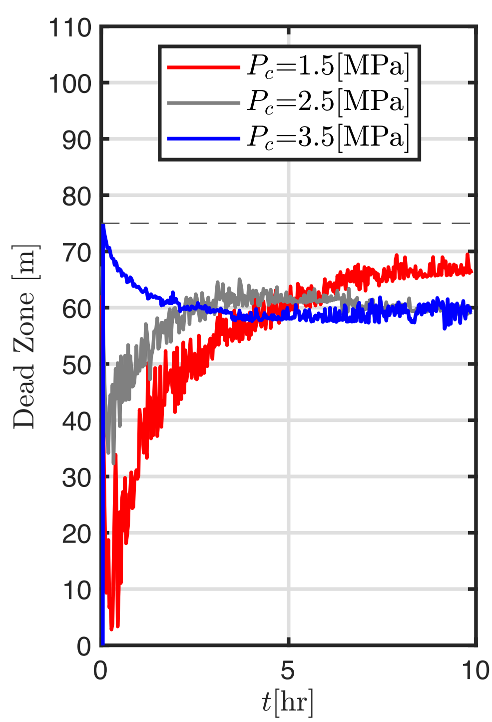

Fig. 13. Extent of dead zone in the thermosyphon at different charge pressures through the first 10 h of operation - the dashed lines represent the pool surface for all cases.

creases. In the pool active zone, heat extraction changes rapidly in the first few hours of operation, as can be seen in Fig. 14(b). However, higher charge pressure extracts more heat after a certain period as steady-state is reached faster, as discussed in the previous paragraph. In regards to the dead zone, lower charge pressures extracts more heat due to the lower associated initial temperature - which is set according to the charge pressure - as shown in Fig. 14(c). Overall, lower charge pressure extracts more heat, mainly because the dead-zone. Nevertheless, the three scenarios are expected to be equal as the simulations reach steady state, due to the exponential decrease of heat extraction in the dead-zone. In the active pool zone, decreasing the charge pressure delays latent heat extraction, as can be seen in Fig. 15(a–c). As for the film zone, it is observed again that the sensible heat extraction is more dominant compared to the latent heat extraction. At lower charge pressure, it is observed that the latent heat extraction approaches zero in the first few hours - implying an absence of the film, as already discussed in Figs. 12(a) and 14(a).

4.4. Impact of wind temperature

The last parameter investigated in this study is the wind temperature. Three different wind temperatures are investigated: 1) $T_{air} = -15[^{\circ}C]$, 2) $T_{air} = -20[^{\circ}C]$, and 3) $T_{air} = -30[^{\circ}C]$. Evidently, lower wind temperature increases the condensation rate, which in turn increases the evaporation and heat extraction rate, especially after longer periods, as shown in Fig. 16. The dead-zone is also shrunk at lower wind temperature, as observed in Fig. 17, af-

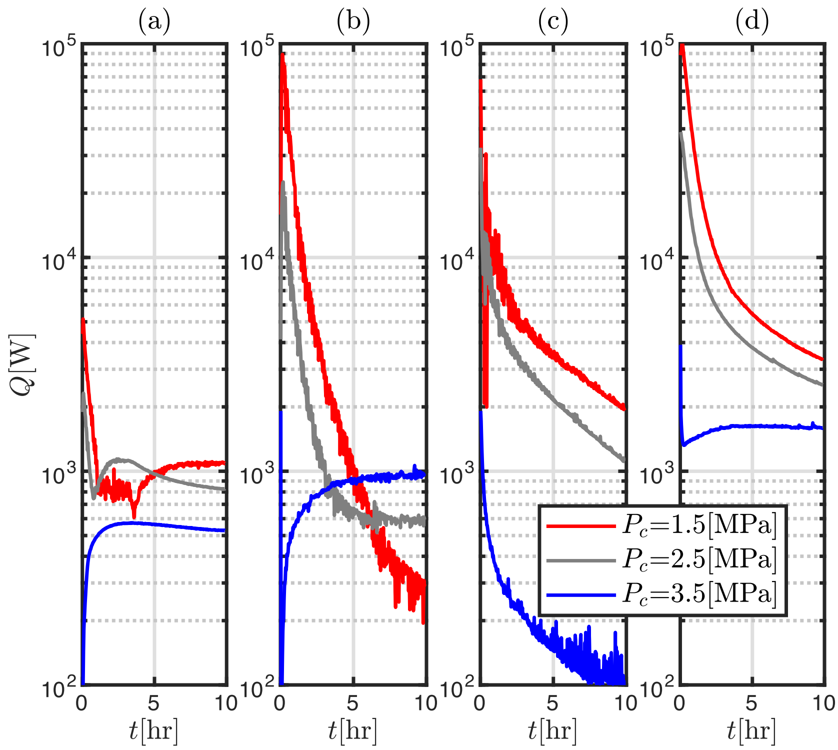

Fig. 14. Heat transfer rate at different charge pressures in the a) film zone, b) active pool zone, and c) dead pool zone, in addition to the d) total heat transfer rate.

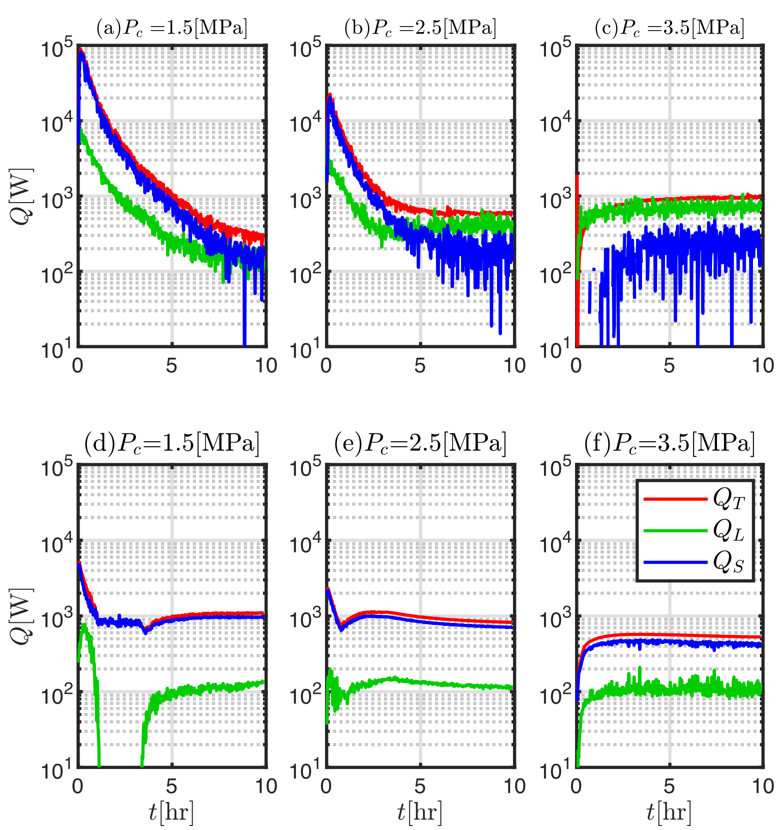

Fig. 15. Modes of heat transfer at different charge pressures where Q_S, Q_L, and Q_T represent sensible heat transfer, latent heat transfer, and total heat transfer, respectively. subplots (a-c) are calculated at the active pool zone, whereas subplots (d-f) are calculated at the film zone.

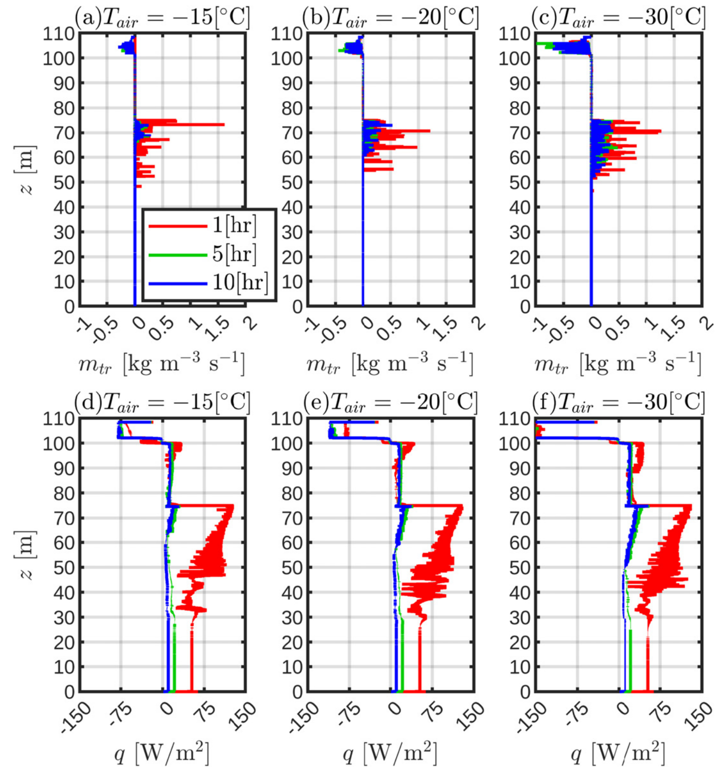

Fig. 16. Mass transfer rate and heat flux along the thermosyphon wall at different wind temperatures (positive mass transfer rate denotes evaporation while negative mass transfer rate represents condensation). The red, green, and blue lines are plotted after one hour, five hours, and 10 h of operation, respectively. (For interpretation of the references to colour in this figure legend, the reader is referred to the web version of this article.)

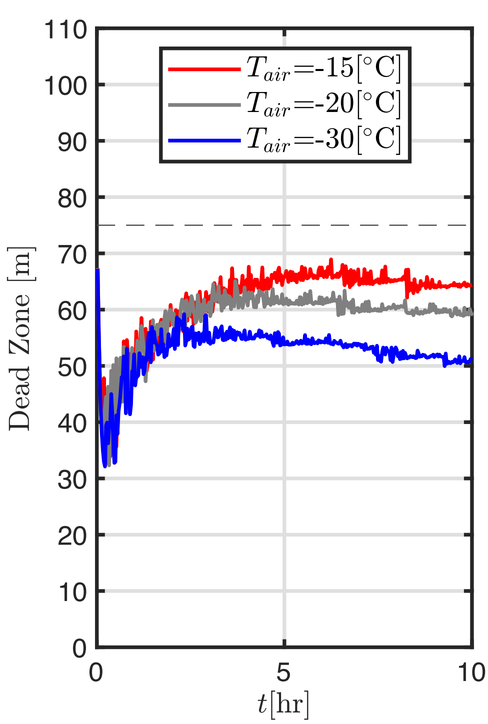

Fig. 17. Extent of dead zone in the thermosyphon at different wind temperatures through the first 10 h of operation - the dashed lines represent the pool surface for all cases.

ter three hours of operation. This is attributed to the cooler feedback from the condenser, which in turn decreases the temperature of CO_2 below the saturation temperature. Overall, the cooler the air temperature, the lower the feedback temperature from the condenser, resulting in higher heat extraction capacity of thermosyphons in all zones - except for the dead-zone, as shown in Fig. 18. The deadzone is too far from the pool surface to be affected by the wind temperature in the first ten hours. Lastly, the mode of heat extraction is qualitatively similar in all scenarios, as shown in Fig. 19, but quantitatively different.

5. Conclusion

In this study, a CFD model is developed for super-long thermosyphons in artificial ground freezing (AGF) applications. The CFD model couples liquid/vapor mass transfer inside the thermosyphon with two-phase heat diffusion within the ground. Particularly, a novel *heterogeneous* mass transfer model is derived considering two main aspect: 1) bubble nucleation temperature is set according to kinetic energy theory and 2) bubble nucleation site is formed at the thermosyphon wall only. Furthermore, as the hydrostatic-pressure profile varies significantly across deep thermosyphons, the saturation temperature is modeled as pressure-dependent. This creates three unique heat extraction zones in the evaporator: 1) film zone above pool surface, 2) active pool zone where bubbles are nucleated, and 3) dead pool zone without boiling.

Following mathematical derivation, the model has been validated and then extended to field conditions. Three different parameters associated to AGF have been considered: 1) the filling ratio of the thermosyphons, 2) the charge pressure of the thermosyphon, and 3) the wind temperature. The following observations are interpreted from the results:

- The extent of the active zone is 10–25 m from the pool surface. Below this distance, a dead-zone is observed.

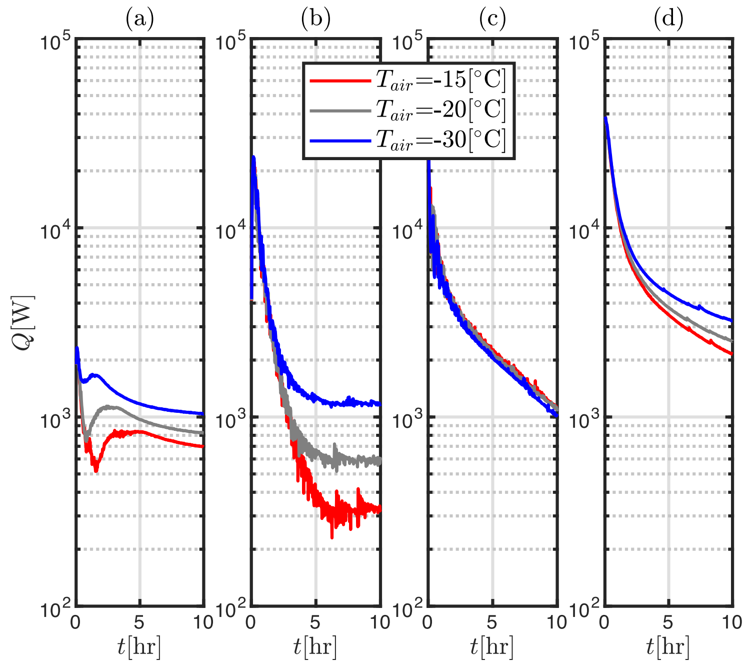

Fig. 18. Heat transfer rate at different wind temperatures in the a) film zone, b) active pool zone, and c) dead pool zone, in addition to the d) total heat transfer rate.

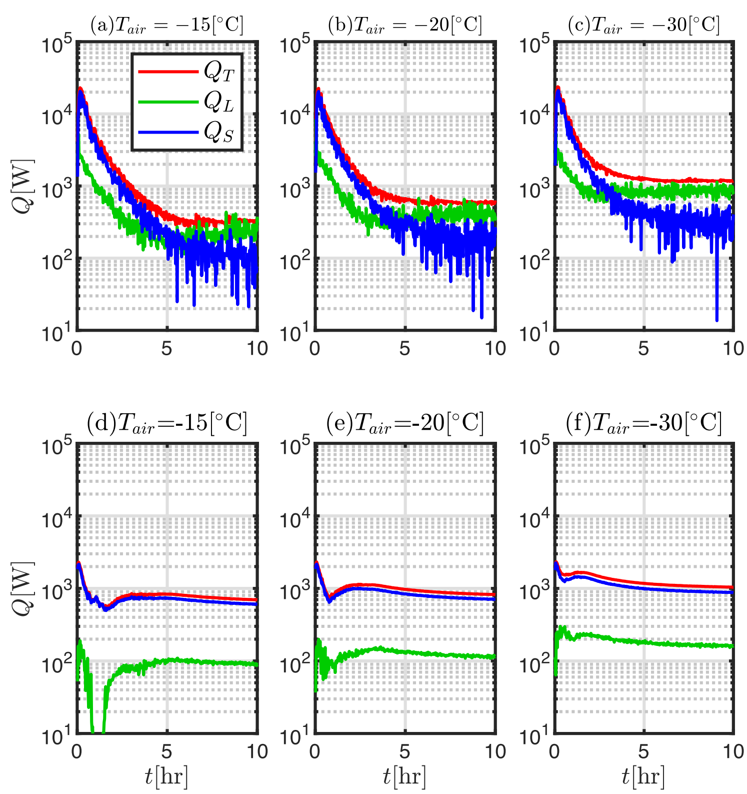

Fig. 19. Modes of heat transfer at different wind temperatures where Q_S, Q_L, and Q_T represent sensible heat transfer, latent heat transfer, and total heat transfer, respectively. subplots (a) though (c) are calculated at the active pool zone, whereas subplots (d) through (f) are calculated at the film zone.

- In the film zone, sensible heat extraction dominates throughout the operation of the thermosyphon.
- At low initial charge pressure, heat extraction capacity of the thermosyphon is high due to the corresponding low initial temperature of the pool. On the other hand, at high initial charge pressure, the heat extraction capacity of the thermosyphon is lower due to the corresponding high initial temperature of the pool. Nevertheless, the effect of the initial charge pressure seems to fade away after around 10 h of operation.
- Lower wind temperature increases the heat extraction capacity in the film zone and the active pool zone.

In our future work, we aim to investigate the impact of other technological difficulties such thermosyphon inclination. Further, we will use this dynamic analysis of deep thermosyphons to verify reduced-order models that feature higher computational efficiency. The reduced-order models will be implemented to analyze deep thermosyphon applications over long periods (years) considering the seasonal temperature.

Declaration of Competing Interest

The authors declare that there is no conflict of interest.

CRediT authorship contribution statement

Ahmad F. Zueter: Conceptualization, Formal analysis, Investigation, Resources, Writing – review & editing, Supervision, Project administration, Funding acquisition. **Muhammad S.K. Tareen:** Formal analysis, Investigation, Writing – review & editing. **Greg Newman:** Formal analysis, Investigation, Writing – review & editing. **Agus P. Sasmito:** Conceptualization, Formal analysis, Investigation, Resources, Writing – review & editing, Supervision, Project administration, Funding acquisition.

Data availability

Data will be made available on request.

Acknowledgments

The authors would like to thank the FRQNT Development Durable du Secteur Minier - II (2020-MN-284402) and Ultra Deep Mining Network (UDMN) (241695 Tri-Council (NCE - UDMN) 2-003). The first author wishes to thank the McGill Engineering Doctoral Award (MEDA) and the FRQNT Doctoral award (Grant No. 2021-B2X-306519).

References

[1] J.P. Zarling, F.D. Haynes, Thermosyphon-based designs and applications for foundations built on permafrost, in: Society of Petroleum Engineers - International Arctic Technology Conference, Anchorage, 1991, pp. 449–458, doi:10.2523/22114-ms.
[2] H. Ma, Heat Pipes, John Wiley & Sons, New Jersey, 2006.
[3] E. Long, Means for maintaining permafrost foundations, 1965,
[4] E. Long, T.L. Thermopile, 1963, First International Conference on Permafrost, Lafayette, 487–491
[5] C.E. Heuer, Application of heat pipes on the trans-alaska pipeline, Tech. Rep. 79-26, 1979.
[6] B. Zhang, Y. Sheng, J. Chen, J. Li, In-situ test study on the cooling effect of two-phase closed thermosyphon in marshy permafrost regions along the Chaidaer-Muli Railway, Qinghai Province, China, 2011, 10.1016/j.coldregions.2010.10.012.
[7] H. Yandong, W. Qingbai, D. Jianhua, L. Jing, Z. Mingli, Y. Zeguo, Numerical simulation of efficient cooling by coupled RR and TCPT on railway embankments in permafrost regions, Appl. Therm. Eng. 133 (2018) 351–360.
[8] W. Zhi, S. Yu, M. Wei, Q. Jilin, J.C. Wu, Z. Wen, Y. Sheng, W. Ma, J.L. Qi, J.C. Wu, Analysis on effect of permafrost protection by two-phase closed thermosyphon and insulation jointly in permafrost regions, Cold Reg. Sci. Technol. 43 (3) (2005) 150–163.
[9] Q. Yu, Z. Zhang, G. Wang, L. Guo, X. Wang, P. Wang, Z. Bao, Analysis of tower foundation stability along the Qinghai–Tibet power transmission line and impact of the route on the permafrost, Cold Reg. Sci. Technol. 121 (2016) 205–213, doi:10.1016/j.coldregions.2015.06.015.
[10] L. Guo, Y. Xie, Q. Yu, Y. You, X. Wang, X. Li, Displacements of tower foundations in permafrost regions along the Qinghai–Tibet power transmission line, Cold Reg. Sci. Technol. 121 (2016) 187–195, doi:10.1016/j.coldregions.2015.07.012.
[11] Crown Indigenous Relations and Northen Affiars Canada, Giant Mine Remediation Project-Arsenic Trioxide Frozen Shell Management and Monitoring Plant-Tech. rep., 2021.
[12] B. Abdalla, C. Fan, C. Mckinnon, V. Gaffard, Numerical study of thermosyphon protection for frost heave, in: ASME 2015 34th International Conference on Ocean, Vol. 5A, 2015, pp. 1–6. Newfoundland
[13] B.A. Abdalla, H. Mei, C. McKinnon, V. Gaffard, Numerical evaluation of permafrost thawing in arctic pipelines and mitigation strategies, in: Arctic Technology Conference 2016, 2016. Newfoundland
[14] M. Zhang, Y. Lai, J. Zhang, Z. Sun, Numerical study on cooling characteristics of two-phase closed thermosyphon embankment in permafrost regions, Cold Reg. Sci. Technol. 65 (2) (2011) 203–210.
[15] W. Pei, M. Zhang, Z. Yan, S. Li, Y. Lai, Numerical evaluation of the cooling performance of a composite l-shaped two-phase closed thermosyphon (LTPCT) technique in permafrost regions, Sol. Energy 177 (2019) 22–31.
[16] W. Pei, M. Zhang, Y. Lai, Z. Yan, S. Li, Evaluation of the ground heat control capacity of a novel air-l-shaped TPCT-ground (ALTG) cooling system in cold regions, Energy 179 (2019) 655–668.
[17] P. Yang, Numerical analysis and application research of heat pipe to solve soil frost heaving problem, J. East China Jiaotong Univ. 15 (4) (1998).
[18] W. Cunzhen, S. Zhijian, P. Yang, Theoritic study on the technology of applying heat pipe to solving frost heaving, Chin. J. Geotech. Eng. 24 (3) (2002) 347–350.
[19] P. Yang, W. Cunzhen, Numerical investigations and engineering applications on freezing expansion of soil restrained two-phase closed thermosyphons, Int. J. Therm. Sci. 41 (4) (2002) 341–347.
[20] A.F. Zueter, G. Newman, A.P. Sasmito, Numerical study on the cooling characteristics of hybrid thermosyphons: case study of the giant mine, Canada, Cold Reg. Sci. Technol. 189 (2021) 103313, doi:10.1016/j.coldregions.2021.103313.
[21] A.D. Atrens, H. Gurgenci, V. Rudolph, CO2 thermosiphon for competitive geothermal power generation, Energy Fuels 23 (1) (2009) 553–557.
[22] A. Franco, M. Vaccaro, On the use of heat pipe principle for the exploitation of medium-low temperature geothermal resources, Appl. Therm. Eng. 59 (1–2) (2013) 189–199.
[23] H. Liu, X. Wang, L. Zheng, H. Yao, Y. Zhu, Y. Wang, Temperature response and thermal performance analysis of a super-long flexible thermosyphon for shallow geothermal utilization: field test and numerical simulation, Int. J. Heat Mass Transf. 192 (2022) 122915, doi:10.1016/j.ijheatmasstransfer.2022.122915.
[24] N. Lamaison, C.L. Ong, J.B. Marcinichen, J.R. Thome, Two-phase mini-thermosyphon electronics cooling: dynamic modeling, experimental validation and application to 2u servers, Appl. Therm. Eng. 110 (2017) 481–494.
[25] C.-C. Chang, S.-C. Kuo, M.-T. Ke, S.L. Chen, Two-phase closed-loop thermosyphon for electronic cooling, Exp. Heat Transf. 23 (2) (2010) 144–156.
[26] T.-E. Tsai, H.-H. Wu, C.-C. Chang, S.L. Chen, Two-phase closed thermosyphon vapor-chamber system for electronic cooling, Int. Commun. Heat Mass Transf. 37 (5) (2010) 484–489.
[27] A. Alizadehdakhel, M. Rahimi, A.A. Alsairafi, CFD modeling of flow and heat transfer in a thermosyphon, Int. Commun. Heat Mass Transf. 37 (3) (2010) 312–318, doi:10.1016/j.icheatmasstransfer.2009.09.002.
[28] C.W. Hirt, B.D. Nichols, Volume of fluid (VOF) method for the dynamics of free boundaries, J. Comput. Phys. 39 (1) (1981) 201–225.
[29] S.C.K. De Schepper, G.J. Heynderickx, G.B. Marin, Modeling the evaporation of a hydrocarbon feedstock in the convection section of a steam cracker, Comput. Chem. Eng. 33 (1) (2009) 122–132.
[30] B. Fadhl, L.C. Wrobel, H. Jouhara, Numerical modelling of the temperature distribution in a two-phase closed thermosyphon, Appl. Therm. Eng. 60 (1–2) (2013) 122–131, doi:10.1016/j.applthermaleng.2013.06.044.
[31] B. Fadhl, L.C. Wrobel, H. Jouhara, CFD modelling of a two-phase closed thermosyphon charged with r134a and r404a, Appl. Therm. Eng. 78 (2015) 482–490, doi:10.1016/j.applthermaleng.2014.12.062.
[32] Z. Xu, Y. Zhang, B. Li, C.C. Wang, Y. Li, The influences of the inclination angle and evaporator wettability on the heat performance of a thermosyphon by simulation and experiment, Int. J. Heat Mass Transf. 116 (2018) 675–684, doi:10.1016/j.ijheatmasstransfer.2017.09.028.
[33] V. Kamburova, A. Ahmedov, I.K. Iliev, I. Beloev, I.R. Pavlović, Numerical modelling of the operation of a two-phase thermosyphon, Therm. Sci. 22 (2018), doi:10.2298/TSCI18S5311K. S1311–S1321
[34] B. Abdullahi, A. El-Sayed, R.K. Al-Dadah, S. Mahmoud, A.F. Mahrous, N.M. Muhammad, S.B. Abbakar, Experimental and numerical investigation of thermosyphon heat pipe performance at various inclination angles, J. Adv. Res. Fluid Mech.Therm. Sci. 44 (1) (2018) 85–98.
[35] H. Jouhara, B. Fadhl, L.C. Wrobel, Three-dimensional CFD simulation of geyser boiling in a two-phase closed thermosyphon, Int. J. Hydrogen Energy 41 (37) (2016) 16463–16476, doi:10.1016/j.ijhydene.2016.02.038.
[36] K. Kafeel, A. Turan, Axi-symmetric simulation of a two phase vertical thermosyphon using Eulerian two-fluid methodology, 2013.
[37] X. Wang, Y. Wang, H. Chen, Y. Zhu, A combined CFD/visualization investigation of heat transfer behaviors during geyser boiling in two-phase closed thermosyphon, Int. J. Heat Mass Transf. 121 (2018) 703–714.
[38] X. Wang, H. Yao, J. Li, Y. Wang, Y. Zhu, Experimental and numerical investigation on heat transfer characteristics of ammonia thermosyhpons at shallow geothermal temperature, Int. J. Heat Mass Transf. 136 (2019) 1147–1159.
[39] X. Wang, Y. Zhu, Y. Wang, Development of pressure-based phase change model for CFD modelling of heat pipesInt. J. Heat Mass Transf., 2019b, 145, 118763, 10.1016/j.ijheatmasstransfer.2019.118763,
[40] M. Knudsen, The cosine law in the kinetic theory of gases, National Aeronautics and Space Administration, 1967.
[41] X. Wang, H. Liu, Y. Wang, Y. Zhu, CFD simulation of dynamic heat transfer behaviors in super-long thermosyphons for shallow geothermal application, Appl. Therm. Eng. 174 (2020) 115295, doi:10.1016/j.applthermaleng.2020.115295.
[42] A. Zueter, A. Nie-Rouquette, M.A. Alzoubi, A.P. Sasmito, Thermal and hydraulic analysis of selective artificial ground freezing using air insulation: experiment and modeling, Comput. Geotech. 120 (2020) 103416.
[43] A.F. Zueter, M. Xu, M.A. Alzoubi, A.P. Sasmito, Development of conjugate reduced-order models for selective artificial ground freezing: thermal and computational analysis, Appl. Therm. Eng. 190 (2021) 116782.
[44] M.A. Alzoubi, A. Nie-Rouquette, A.P. Sasmito, Conjugate heat transfer in artificial ground freezing using enthalpy-porosity method: experiments and model validation, Int. J. Heat Mass Transf. 126 (2018) 740–752.
[45] A.F. Zueter, A.G. Madiseh, F.P. Hassani, A.P. Sasmito, Effect of freeze pipe eccentricity in selective artificial ground freezing applications, ASME J. Therm. Sci. Eng.Appl. 14 (2022) 011015.

[46] National Institute of Standards and Technology, NIST chemistry webbook, 2018. https://www.webbook.nist.gov/

[47] SRK Consulting (Canada) Inc., Freeze Optimization Study Update for MVEIRB and Parties Aboriginal Affairs and Northern Development Freeze Optimization Study Update for MVEIRB and PartiesTech. Rep. August, Ottawa, 2012.

[48] V. Guichet, S. Almahmoud, H. Jouhara, Nucleate pool boiling heat transfer in wickless heat pipes (two-phase closed thermosyphons): a critical review of correlations, Therm. Sci. Eng. Prog. 13 (2019) 100384.

[49] W.M. Rohsenow, J.P. Hartnett, Y.I. Cho, Handbook of Heat Transfer, Vol. 3, McGraw-Hill, New York, 1998.

[50] M. Noel, D. Hockley, Thermal analysis of an experimental thermosyphon installed at the giant mine in yellowknife, NT, Canada, in: 57th Canadian Geotechnical Conference and 5th joint CGS-IAH Conference, Quebec, 2004.

[51] A.F. Zueter, S. Akhtar, A.P. Sasmito, Uncertainty analysis of operational conditions in selective artificial ground freezing applications, J. Sustain. Min 14 (2022) 169–179.